LETTER

Relativistic boost as the cause of periodicity in a massive black–hole binary candidate

Daniel J. D'Orazio[1], Zoltán Haiman[1] & David Schiminovich[1]

Because most large galaxies contain a central black hole, and galaxies often merge[1], black-hole binaries are expected to be common in galactic nuclei[2]. Although they cannot be imaged, periodicities in the light curves of quasars have been interpreted as evidence for binaries[3–5], most recently in PG 1302-102, which has a short rest-frame optical period of four years (ref. 6). If the orbital period of the black-hole binary matches this value, then for the range of estimated black-hole masses, the components would be separated by 0.007–0.017 parsecs, implying relativistic orbital speeds. There has been much debate over whether black-hole orbits could be smaller than one parsec (ref. 7). Here we report that the amplitude and the sinusoid-like shape of the variability of the light curve of PG 1302-102 can be fitted by relativistic Doppler boosting of emission from a compact, steadily accreting, unequal-mass binary. We predict that brightness variations in the ultraviolet light curve track those in the optical, but with a two to three times larger amplitude. This prediction is relatively insensitive to the details of the emission process, and is consistent with archival ultraviolet data. Follow-up ultraviolet and optical observations in the next few years can further test this prediction and confirm the existence of a binary black hole in the relativistic regime.

Assuming PG 1302-102 is a binary, it is natural to attribute its optical emission to gas that is bound to each black hole, forming circumprimary and circumsecondary accretion flows. Such flows, which form 'minidisks', are generically found in high-resolution two- and three-dimensional hydrodynamic simulations that include the black holes in their simulated domain[8–15]. Assuming a circular orbit, the velocity of the lower-mass secondary black hole is

$$v_2 = \left(\frac{2\pi}{1+q}\right)\left(\frac{GM}{4\pi^2 P}\right)^{1/3} = 8{,}500\left(\frac{1.5}{1+q}\right)\left(\frac{M}{10^{8.5} M_\odot}\right)^{1/3}\left(\frac{P}{4.04\,\text{yr}}\right)^{-1/3}\,\text{km s}^{-1}$$

or approximately $0.03c$ for the fiducial parameters chosen in the parentheses on the right ($q = 0.5$, $M = 10^{8.5} M_\odot$, $P = 4.04$ yr), where $M = M_1 + M_2$ is the total binary mass, $M_{1,2}$ are the individual masses, $q = M_2/M_1 \leq 1$ is the mass ratio, $M_\odot$ is the mass of the Sun, P is the orbital period, G is the gravitational constant, and c is the speed of light. The orbital velocity of the higher-mass primary black hole is $v_1 = qv_2$. Even if a minidisk has a steady intrinsic rest-frame luminosity, its apparent flux on Earth is modulated by relativistic Doppler beaming. The photon frequencies suffer relativistic Doppler shift by the factor $D = \left[\Gamma\left(1 - \beta_\parallel\right)\right]^{-1}$, where $\Gamma = (1 - \beta^2)^{-1/2}$ is the Lorentz factor, $\beta = v/c$ is the three-dimensional velocity v in units of the speed of light c, and $\beta_\parallel = \beta\cos(\varphi)\sin(i)$ is the component of the velocity along the line of sight, with i and φ the orbital inclination and phase, respectively. Because the photon phase-space density, which is proportional to F_ν/ν^3, is invariant in special relativity, the apparent flux F_ν at a fixed observed frequency ν is modified from the flux of a stationary source F_ν^0 to $F_\nu = D^3 F_{D^{-1}\nu}^0 = D^{3-\alpha}F_\nu^0$. The last step assumes an intrinsic power-law spectrum $F_\nu^0 \propto \nu^\alpha$. To first order in ν/c, this assumption causes a sinusoidal modulation of the apparent flux along the orbit, by a fractional amplitude $\Delta F_\nu/F_\nu = \pm(3 - \alpha)\nu\cos(\varphi/c)\sin(i)$. Although

light-travel time modulations appear at the same order, they are subdominant to the Doppler modulation. This modulation is analogous to periodic modulations from relativistic Doppler boost predicted[16] and observed for extrasolar planets[17,18] and for a double white-dwarf binary[19], but here it has a much higher amplitude.

The light curve of PG 1302-102 is well measured over approximately two periods (approximately 10 yr). The amplitude of the variability is ± 0.14 mag (measured in the optical V band[20]), which corresponds to $\Delta F_\nu/F_\nu = \pm 0.14$. The spectrum of PG 1302-102 in and around the V band is well approximated by a double power-law, with $\alpha \approx 0.7$ (between 0.50 μm and 0.55 μm) and $\alpha \approx 1.4$ (between 0.55 μm and 0.6 μm), except for small deviations caused by broad lines. We obtain an effective single slope $\alpha_{\text{opt}} = 1.1$ over the entire V band. We conclude that the 14% variability can be attributed to relativistic beaming for a line-of-sight velocity amplitude of $v\sin(i) = 0.074c = 22{,}000$ km s^{-1}.

Although large, this velocity can be realized for a massive (high-M) but unequal-mass (low-q) binary, whose orbit is viewed not too far from edge-on (high $\sin(i)$). In Fig. 1, we show the required combination of these three parameters that would produce a 0.14-mag variability in the sum-total of Doppler-shifted emission from the primary and the secondary black hole. As this figure shows, the required mass is $\gtrsim 10^{9.1} M_\odot$, consistent with the high end of the range that has been inferred for PG 1302-102. The orbital inclination can be in the range $i = 60°–90°$. The mass ratio q has to be low, $q \lesssim 0.3$, which is consistent with expectations based on cosmological galaxy merger models[21], and also with the identification of the optical and binary periods (for $q \gtrsim 0.3$, hydrodynamic simulations predict that the mass-accretion rates fluctuate with a period several times longer than the orbital period[22]).

As Fig. 1 shows, fully accounting for the observed optical variability also requires that the bulk of the optical emission arises from gas bound to the faster-moving secondary black hole ($f_2 \gtrsim 80\%$). We find that this condition is naturally satisfied for unequal-mass black holes. Hydrodynamic simulations have shown that for $0.03 \lesssim q \lesssim 0.1$, the accretion rate onto the secondary black hole is a factor of 10–20 higher than that onto the primary[13]. Because the secondary captures most of the accreting gas from the circumbinary disk, the primary is 'starved', and radiates with a much lower efficiency. In the (M, q) ranges favoured by the beaming scenario, we find that the primary contributes less than 1% to the total luminosity, and the circumbinary disk contributes less than 20%, leaving the secondary as the dominant source of emission in the three-component system (see Methods).
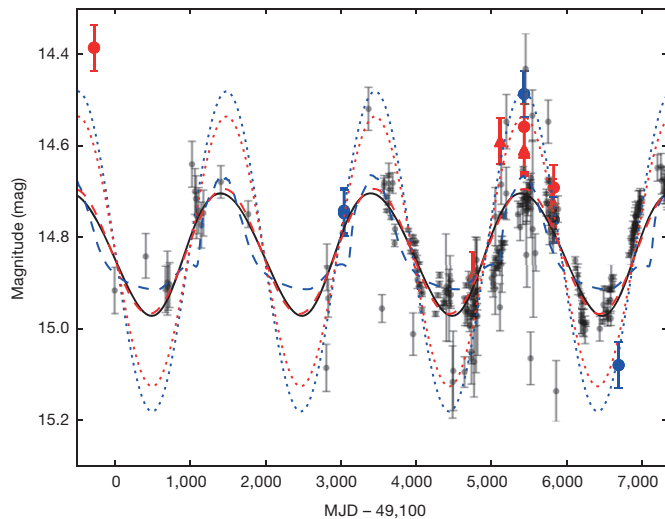
The optical light curve of PG 1302-102 appears remarkably sinusoidal compared to that of the best-studied previous quasi-periodic quasar binary black-hole candidate, which shows periodic bursts[4]. Nevertheless, the light-curve shape deviates from a pure sinusoid. To see if such deviations naturally arise within our model, we maximized the Bayesian likelihood over five parameters (period P, velocity amplitude K, eccentricity e, argument of pericentre ω, and an arbitrary reference time t_0) of a Kepler orbit[23] and fitted the observed optical light curve. In this procedure, we accounted for additional stochastic physical variability with a broken-power-law power spectrum

[1]Department of Astronomy, Columbia University, 550 West 120th Street, New York, New York 10027, USA.
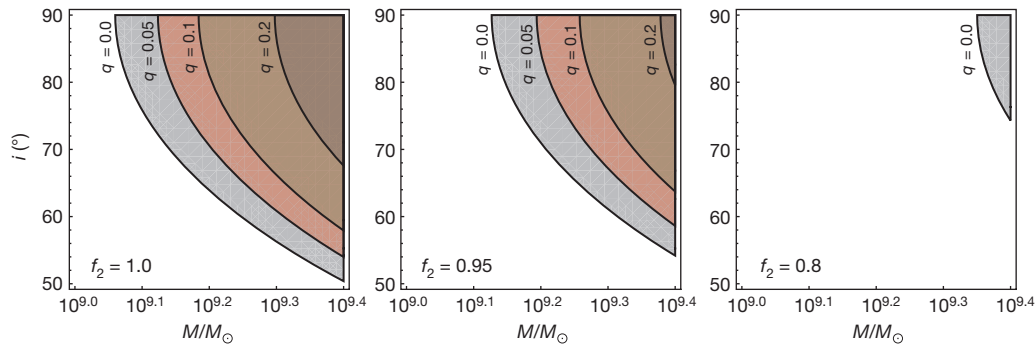
Figure 1 | Binary parameters producing the optical flux variations of PG 1302-102 by relativistic boost. Combinations of total binary mass M, mass ratio $q = M_2/M_1$, and inclination i that cause $>13.5\%$ flux variability (or line-of-sight velocity amplitude $(v/c)\sin(i) \gtrsim 0.07$) in the emission from the primary and secondary black holes, computed from the Doppler factor $D^{3-\alpha}$ with the effective spectral slope of $\alpha_{opt} = 1.1$ in the V band. The solid lines corre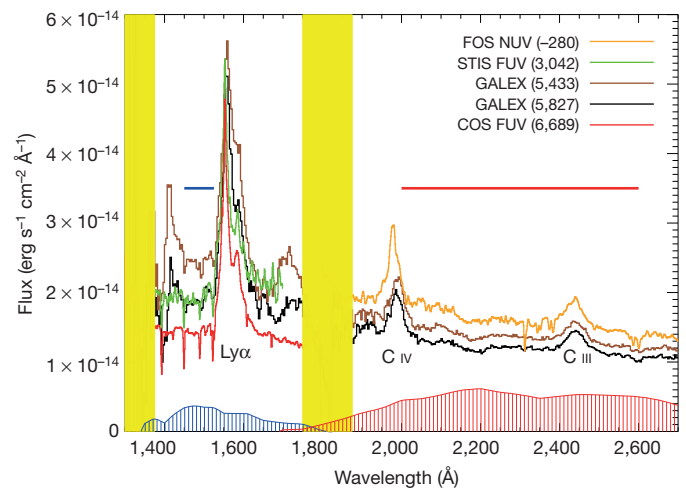spond to different values of q as labelled; the shaded regions correspond to intermediate values. We assume that a fraction $f_2 = 1.0$, 0.95, or 0.8 of the total luminosity arises from the secondary black hole; these values are consistent with fractions found in hydrodynamic simulations[13] (see Methods). The inclination angle is defined such that $i = 0°$ corresponds to a face-on view of PG 1302-102, and $i = 90°$ corresponds to an edge-on view.

(a 'damped random walk'[24]) described by two additional parameters. This analysis returns a best-fit with a non-zero eccentricity of $e = 0.09^{+0.07}_{-0.06}$, although a Bayesian criterion does not favour this model over a pure sinusoid with fewer parameters (see Methods). We considered an alternative model to explain optical variability of PG 1302-102, in which the luminosity variations track the fluctuations in the mass-accretion rate that is predicted in hydrodynamic simulations[9–11,13,25]. However, the amplitude of these hydrodynamic fluctuations are large (order one), and their shape is 'bursty' rather than sinusoid-like[11,13,15]; as a result, we find that they provide a poorer fit to the observations (see Fig. 2 and Methods). Furthermore, for mass ratios $q \gtrsim 0.05$, hydrodynamic simulations predict a characteristic pattern of periodicities at multiple frequencies, but an analysis of the periodogram of PG 1302-102 has not uncovered evidence for multiple peaks[26].

A simple observational test of relativistic beaming is possible, owing to the strong frequency dependence of the spectral slope of PG 1302-102: $\alpha = \mathrm{dln}(F_\nu)/\mathrm{dln}(\nu)$. The continuum spectrum of PG 1302-102 is nearly flat with a slope $\beta_{FUV} \equiv \mathrm{dln}(F_\lambda)/\mathrm{dln}(\lambda) = 0$ in the far-ultraviolet (FUV; 0.145–0.1525 μm) band, where F_λ is the apparent flux at an observed wavelength λ, and shows a tilt with $\beta_{NUV} = -0.95$ in the near-ultraviolet (NUV; 0.20–0.26 μm) range; see Fig. 3 and Methods. These slopes translate to $\alpha_{FUV} = -2$ and $\alpha_{NUV} = -1.05$ in the respective bands, compared to $\alpha_{opt} = 1.1$ in the optical. The UV emission can be attributed to the same minidisks that are responsible for the optical light, and would therefore share the same Doppler shifts in frequency. These Doppler shifts would translate into UV variability that is larger by a factor of $(3 - \alpha_{FUV})/(3 - \alpha_{opt}) = 5/1.9 = 2.63$ and $(3 - \alpha_{NUV})/(3 - \alpha_{opt}) = 4.05/1.9 = 2.13$ compared to the optical, and reaches maximum amplitudes of $\pm37\%$ (FUV) and $\pm30\%$ (NUV).

Figure 2 | The optical and ultraviolet light curves of PG 1302-102. The grey filled circles with 1σ errors are the optical data[6], superimposed with a best-fit sinusoid (red dashed curve). The solid black curve is the best-fit relativistic light-curve. The blue dashed curve is the best-fit model that was obtained by scaling the mass-accretion rate determined from a hydrodynamic simulation of an unequal-mass ($q = 0.1$) binary[11]. The red and blue filled circles with 1σ errors correspond to archival NUV (red) and FUV (blue) spectral observations; the red filled triangles (with 1σ errors) represent archival photometric NUV data (see Fig. 3). The UV data include an arbitrary overall normalization to match the mean optical brightness. The red and blue dotted curves are the best-fit relativistic optical light curves with amplitudes scaled up by factors of 2.17 and 2.57, which best match the NUV and FUV data, respectively. MJD, modified Julian day.

Figure 3 | Archival UV spectra of PG 1302-102 from 1992–2011. FUV and NUV spectra obtained by instruments on the HST and by GALEX, as labelled. COS, cosmic origins spectrograph; FOS, faint object spectrograph; STIS, space telescope imaging spectrograph. Numbers in brackets are the dates (in MJD − 49,100) the data were collected. Vertical yellow bands mark regions outside the spectroscopic range of both GALEX and the HST and contain no useful spectral data. Assignments of the main peaks are given. Lyα, Lyman α. From each spectrum, average flux measurements (shown in Fig. 2) were computed in one or both of the UV bands over the frequency range indicated by the horizontal bars. The full GALEX photometric band shapes for FUV and NUV photometry are shown for reference as shaded blue and red curves, respectively. Additional GALEX NUV photometric data were also used in Fig. 2. The UV spectra show an offset by as much as $\pm30\%$ relative to one another, close to the value expected from relativistic boost (see Methods).

Five separate UV spectra of PG 1302-102 have been collected between 1992 and 2011, by instruments on the Hubble Space Telescope (HST) and on the Galaxy Evolution Explorer (GALEX) satellite (see Fig. 3); additional photometric observations were taken with GALEX at four different times between 2006 and 2009 (shown in Fig. 2). The brightness variations in both the FUV and NUV bands show variability that resembles the optical variability, but with a larger amplitude. Adopting the parameters of our best-fit sinusoid model, and allowing only the amplitude to vary, we find that the UV data yields best-fit variability amplitudes of $\Delta F_\nu/F_\nu|_{FUV} = \pm(35.0 \pm 3.9)\%$ and $\Delta F_\nu/F_\nu|_{NUV} = \pm(29.5 \pm 2.4)\%$ (shown in Fig. 2). These amplitudes are factors of 2.57 ± 0.28 and 2.17 ± 0.17 higher than in the optical, in excellent agreement with the values 2.63 and 2.13 that are expected from the corresponding spectral slopes.

Relativistic beaming provides a simple and robust explanation of the optical periodicity of PG 1302-102. The prediction that the larger UV variations should track the optical light curve can be tested rigorously in the future with measurements of the optical and UV brightness that are collected at or near the same time, are repeated two or more times, are separated by a few months to about 2 yr, and cover up to half of the optical period. A positive result will constitute the first detection of relativistic massive black-hole binary motion; it will also serve as a confirmation of the binary nature of PG 1302-102, remove the ambiguity in the orbital period, and tightly constrain the binary parameters to be close to those shown in Fig. 1.

Online Content Methods, along with any additional Extended Data display items and Source Data, are available in the online version of the paper; references unique to these sections appear only in the online paper.

1. Kormendy, J. & Ho, L. C. Coevolution (or not) of supermassive black holes and host galaxies. *Annu. Rev. Astron. Astrophys.* **51,** 511–653 (2013).
2. Begelman, M. C., Blandford, R. D. & Rees, M. J. Massive black hole binaries in active galactic nuclei. *Nature* **287,** 307–309 (1980).
3. Komossa, S. Observational evidence for binary black holes and active double nuclei. *Mem. Soc. Astron. Ital.* **77,** 733–741 (2006).
4. Valtonen, M. J. *et al.* A massive binary black-hole system in OJ 287 and a test of general relativity. *Nature* **452,** 851–853 (2008).
5. Liu, T. *et al.* A periodically varying luminous quasar at $z = 2$ from the Pan-STARRS1 Medium Deep Survey: a candidate supermassive black hole binary in the gravitational wave-driven regime. *Astrophys. J.* **803,** L16 (2015).
6. Graham, M. J. *et al.* A possible close supermassive black-hole binary in a quasar with optical periodicity. *Nature* **518,** 74–76 (2015).
7. Milosavljević, M. & Merritt, D. in *The Astrophysics of Gravitational Wave Sources, AIP Conf. Proc.* (eds Centrella, J. M. & Barnes, S.) **686,** 201–210 (AIP, 2003).
8. Hayasaki, K., Mineshige, S. & Ho, L. C. A supermassive binary black hole with triple disks. *Astrophys. J.* **682,** 1134–1140 (2008).
9. Shi, J.-M., Krolik, J. H., Lubow, S. H. & Hawley, J. F. Three-dimensional magnetohydrodynamic simulations of circumbinary accretion disks: disk structures and angular momentum transport. *Astrophys. J.* **749,** 118 (2012).
10. Roedig, C. *et al.* Evolution of binary black holes in self gravitating discs. Dissecting the torques. *Astron. Astrophys.* **545,** A127 (2012).
11. D'Orazio, D. J., Haiman, Z. & MacFadyen, A. Accretion into the central cavity of a circumbinary disc. *Mon. Not. R. Astron. Soc.* **436,** 2997–3020 (2013).
12. Nixon, C., King, A. & Price, D. Tearing up the disc: misaligned accretion on to a binary. *Mon. Not. R. Astron. Soc.* **434,** 1946–1954 (2013).
13. Farris, B. D., Duffell, P., MacFadyen, A. I. & Haiman, Z. Binary black hole accretion from a circumbinary disk: gas dynamics inside the central cavity. *Astrophys. J.* **783,** 134 (2014).
14. Dunhill, A. C., Cuadra, J. & Dougados, C. Precession and accretion in circumbinary discs: the case of HD 104237. *Mon. Not. R. Astron. Soc.* **448,** 3545–3554 (2015).
15. Shi, J.-M. & Krolik, J. H. Three-dimensional MHD simulation of circumbinary accretion disks. II. Net accretion rate. *Astrophys. J.* **807,** 131 (2015).
16. Loeb, A. & Gaudi, B. S. Periodic flux variability of stars due to the reflex Doppler effect induced by planetary companions. *Astrophys. J.* **588,** L117–L120 (2003).
17. van Kerkwijk, M. H. *et al.* Observations of Doppler boosting in Kepler light curves. *Astrophys. J.* **715,** 51–58 (2010).
18. Mazeh, T. & Faigler, S. Detection of the ellipsoidal and the relativistic beaming effects in the CoRoT-3 lightcurve. *Astron. Astrophys.* **521,** L59 (2010).
19. Shporer, A. *et al.* A ground-based measurement of the relativistic beaming effect in a detached double white dwarf binary. *Astrophys. J.* **725,** L200–L204 (2010).
20. Djorgovski, S. G. *et al.* Exploring the variable sky with the Catalina Real-time Transient Survey. In *The First Year of MAXI: Monitoring Variable X-ray Sources* (eds Mihara, T. & Serino, M.) 32 (MAXI, 2010).
21. Volonteri, M., Haardt, F. & Madau, P. The assembly and merging history of supermassive black holes in hierarchical models of galaxy formation. *Astrophys. J.* **582,** 559–573 (2003).
22. D'Orazio, D. J., Haiman, Z., Duffell, P., Farris, B. D. & MacFadyen, A. I. A reduced orbital period for the supermassive black hole binary candidate in the quasar PG 1302–102? *Mon. Not. R. Astron. Soc.* **452,** 2540–2545 (2015).
23. Wright, J. T. & Gaudi, B. S. in *Planets, Stars and Stellar Systems* Vol. 3 (eds Oswalt, T. D. *et al.*) 489–540 (Springer, 2013).
24. Kelly, B. C., Bechtold, J. & Siemiginowska, A. Are the variations in quasar optical flux driven by thermal fluctuations? *Astrophys. J.* **698,** 895–910 (2009).
25. MacFadyen, A. I. & Milosavljević, M. An eccentric circumbinary accretion disk and the detection of binary massive black holes. *Astrophys. J.* **672,** 83–93 (2008).
26. Charisi, M., Bartos, I., Haiman, Z., Price-Whelan, A. & Márka, S. Multiple periods in the variability of the supermassive black hole binary candidate quasar PG1302-102? *Mon. Not. R. Astron. Soc. Lett.* (in the press).

Author Contributions Z.H. conceived and supervised the project, performed the orbital velocity calculations, and wrote the first draft of the paper. D.J.D. computed the emission models and performed the fits to the observed light curve. D.S. analysed the archival UV data. All authors contributed to the text.

METHODS

V-band emission from a three-component system in PG 1302-102. Here we assume that the PG 1302-102 supermassive black-hole (SMBH) binary system includes three distinct luminous components: a circumbinary disk (CBD), as well as actively accreting primary and secondary SMBHs. The optical brightness of each of the three components can be estimated once their accretion rates and the black-hole masses M_1 and M_2 are specified. Using the absolute V-band magnitude of PG 1302-102, $M_V = -25.81$, and applying a bolometric correction BC ≈ 10 (ref. 27), we infer a total bolometric luminosity of $L_{bol} = 6.5(\text{BC}/10) \times 10^{46}\,\text{erg s}^{-1}$. Bright quasars with the most massive SMBHs ($M \gtrsim 10^9 M_\odot$), have a typical radiative efficiency of $\epsilon = 0.3$ (ref. 28). Adopting this value, the implied accretion rate is $\dot{M} = L_{bol}/(\epsilon c^2) = 3.7 M_\odot \text{yr}^{-1}$ (where the overdot indicates differentiation with respect to time).

We identify this as the total accretion rate through the CBD, and require that at small radii, the rate is split between the two black holes $\dot{M} = \dot{M}_1 + \dot{M}_2$ with the ratio $\eta \equiv \dot{M}_2/\dot{M}_1$. Hydrodynamic simulations[13] have found that the secondary black hole captures the large majority of the gas, with $10 \lesssim \eta \lesssim 20$ for $0.03 \lesssim q \lesssim 0.1$ (where $q \equiv M_2/M_1$). Defining the Eddington ratio of the ith disk as its accretion rate scaled by its Eddington-limited rate $f_{i,\text{Edd}} \equiv \dot{M}_i + \dot{M}_{i,\text{Edd}}$ with $\dot{M}_{\text{Edd}} \equiv L_{\text{Edd}}/(0.1 c^2)$ (here L_{Edd} is the Eddington luminosity for the ith black hole, and we have adopted the fiducial radiative efficiency of $\epsilon = 0.1$ to be consistent with the standard definition in the literature), we have

$$f_{\text{CBD,Edd}} \approx 0.068 \left(\frac{M}{10^{9.4} M_\odot}\right)^{-1}$$

$$f_{1,\text{Edd}} = f_{\text{CBD,Edd}} \frac{1+q}{1+\eta} \approx 0.0034 \left(\frac{f_{\text{CBD,Edd}}}{0.068}\right)\left(\frac{1+q}{1.05}\right)\left(\frac{21}{1+\eta}\right)$$

$$f_{2,\text{Edd}} = \eta \frac{f_{1,\text{Edd}}}{q} \approx 1.37 \left(\frac{f_{1,\text{Edd}}}{0.0034}\right)\left(\frac{\eta}{20}\right)\left(\frac{0.05}{q}\right)$$

where the subscripts 1 and 2 refer to the primary and the secondary black holes, respectively. We adopt a standard, radiatively efficient, geometrically thin, optically thick Shakura–Sunyaev disk model[29] to compute the luminosities produced in the CBD and the circumsecondary disk (CSD). Although the secondary black hole is accreting at a super-Eddington rate, recent three-dimensional radiation magnetohydrodynamic simulations of super-Eddington accretion find radiative efficiencies comparable to the values in standard thin-disk models[30]. On the other hand, the primary black hole is accreting below the critical rate $\dot{M}_1 \lesssim \dot{M}_{\text{ADAF}} \approx 0.027 (\alpha/0.3)^2 \dot{M}_{\text{Edd}}$ (ADAF, advection-dominated accretion flow; α is the viscosity parameter) at which advection dominates the energy balance[31]. We therefore estimate the luminosity of the primary black hole from a radiatively inefficient ADAF[32,33], rather than from a Shakura–Sunyaev disk. This interpretation is supported by the fact that PG 1302-102 is known to be an extended radio source, with evidence for a jet and bends in the extended radio structure[34], features that are commonly associated with sub-Eddington sources[35].

For the radiatively efficient CBD and CSD, the frequency-dependent luminosity is determined by integrating the local, modified black-body flux over the area of the disk:

$$L_\nu = 2\pi \int_{R_{in}}^{R_{out}} F_\nu [T_p(r)] r\, dr$$

where

$$F_\nu = \pi \frac{2\epsilon_\nu^{1/2}}{1 + \epsilon_\nu^{1/2}} B_\nu, \quad \epsilon_\nu = \frac{\kappa_\nu^{abs}}{\kappa_\nu^{abs} + \kappa^{es}}$$

B_ν is the Planck function, κ_ν^{abs} is the frequency-dependent absorption opacity, κ^{es} is the electron scattering opacity, and $r \in (R_{in}, R_{out})$ is the radial coordinate, with $R_{in,out}$ the inner and outer radii of the appropriate disk. We compute the radial disk-photosphere temperature profile T_p by equating the viscous heating rate with the modified black-body flux:

$$\frac{3GM\dot{M}}{8\pi r^3} \left[1 - \left(\frac{r_{ISCO}}{r}\right)^{1/2}\right] = \zeta(\nu, T_p) \sigma T_p^4$$

where

$$\zeta(\nu, T_p) = \frac{15}{\pi^4} \int \frac{2\epsilon_\nu^{1/2}(x)}{1 + \epsilon_\nu^{1/2}(x)} \frac{x^3 e^{-x}}{1 - e^{-x}} dx, \quad x \equiv \frac{h\nu}{k_B T_p}$$

σ is the Stefan–Boltzmann constant, k_B is the Boltzmann constant, h is the Planck constant, and r_{ISCO} is the radius of the innermost stable circular orbit (ISCO). When solving for the photosphere temperature, we work in the limit that $\kappa_\nu^{abs} \ll \kappa^{es}$ following appendix A of ref. 36, and we adopt $r_{i,\text{ISCO}} = 6GM_i/c^2$, and

$(R_{in}, R_{out}) = (2a, 200a)$ and $(R_{in}, R_{out}) = (r_{2,\text{ISCO}}, a(q/3)^{1/3})$ for the CBD and CSD, respectively. Here the superscript i refers to the ith disk, a is the binary separation, $6GM$ is the location of the ISCO for a Schwarzschild black hole (our results are insensitive to this choice) and $a(q/3)^{1/3}$ is the Hill radius of the secondary black hole (which provides an upper limit on the size of the CSD[37]).

The optical luminosity of an ADAF is sensitive to the assumed microphysical parameters and its computation is more complicated than that for a thin disk. Here we first compute a reference thin-disk luminosity L_{SS} (SS, Shakura–Sunyaev) for the primary black hole, and multiply it by the ratio of the bolometric luminosity of an ADAF to an equivalent thin-disk luminosity from ref. 32:

$$\frac{L_{\text{ADAF}}}{L_{SS}} \approx 0.008 \left(\frac{\dot{M}/\dot{M}_{\text{Edd}}}{0.0034}\right)\left(\frac{\alpha}{0.3}\right)^{-2}$$

For calculating the reference L_{SS}, we adopted parameters that are consistent with ref. 32, in particular, $\epsilon = 0.1$. Although the above ratio is for bolometric luminosities, we find that it agrees well with the factor-of-100 difference in the V band shown in figure 6 of ref. 33, between ADAF and thin-disk spectra, with parameters similar to PG 1302-102 ($10^9 M_\odot$, $\dot{M} = \dot{M}_{\text{ADAF}} = 10^{-1.5} \dot{M}_{\text{Edd}}$, $\alpha \approx 0.3$).

Extended Data Figure 1 shows the thin-disk CBD and CSD spectra for a total Eddington ratio of $f_{\text{CBD,Edd}} = 0.07$, consistent with the high-mass estimates for PG 1302-102 that are needed for the beaming scenario ($M = 10^{9.4} M_\odot$ and $q = 0.05$). The red dot shows the reduced V-band luminosity of an ADAF onto the primary. The secondary clearly dominates the total V-band luminosity, with the primary contributing less than 1%, and the CBD contributing approximately 14%. In practice, the contribution from the CBD becomes non-negligible only for the smallest binary masses and lowest mass ratios (reaching 20% for $M < 10^9 M_\odot$ and $q < 0.025$).

We compute the contributions of each of the three components to the total luminosity, $L_{tot}^V = L_1^V + L_2^V + L_{CBD}^V$, and the corresponding total fractional-modulation amplitude $\Delta L_{tot}^V / L_{tot}^V = (\Delta L_1^V + \Delta L_2^V)/L_{tot}^V$, for each value of the total mass M and mass ratio q. The primary is assumed to be Doppler modulated with a line-of-sight velocity $v_1 = -q v_2$, whereas the emission from the CBD is assumed to be constant over time ($\Delta L_{CBD}^V = 0$). Extended Data Figure 2 shows regions in (M, q, i) parameter space where the total luminosity variation due to relativistic beaming exceeds 14%. This figure recreates Fig. 1 of the main text, but using the luminosity contributions computed self-consistently in the above model, rather than assuming a constant value of f_2. Because the secondary is found to be dominant, the relativistic-beaming scenario is consistent with a wide range of binary parameters.

Model fitting to the PG 1302-102 optical light curve. We fitted models to the observed light curve of PG 1302-102 by maximizing the Bayesian likelihood $\mathcal{L} \propto \det |\text{Cov}^D \text{Cov}^{ph}|^{-1/2} \exp(-\chi^2/2)$, where $\chi^2 \equiv Y^T (\text{Cov})^{-1} Y$ and $Y \equiv O - M$ is the difference vector between the mean flux predicted in a model and the observed flux at each observation time t_i. Here Cov is the covariance matrix of flux uncertainties, allowing for correlations between fluxes measured at different t_i. We include two types of uncertainties: (1) random (uncorrelated) measurement errors

$$\text{Cov}_{ij}^{ph} = \begin{cases} \sigma_i^2 & i = j \\ 0 & i \neq j \end{cases}$$

where σ_i^2 is the variance in the photometric measurement for the ith data point (as reported in ref. 6); and (2) correlated noise due to intrinsic quasar variability, with covariance between the ith and jth data points

$$\text{Cov}_{ij}^D = \sigma_D^2 \exp\left[\frac{-|t_i - t_j|}{(1+z)\tau_D}\right]$$

The parameters σ_D and τ_D determine the amplitude and rest-frame coherence time, respectively, of correlated noise described by the damped random walk model[24], and the factor of $(1+z)$ converts τ_D to the observer's frame where the t_i are measured. The normalization of the Bayesian likelihood depends on these parameters, and therefore the normalization must be included when maximizing the likelihood over these parameters[38]. The covariance matrix for the total noise is given by $\text{Cov} = \text{Cov}^D + \text{Cov}^{ph}$. We assume both types of noise are Gaussian, which provides a good description of observed quasar variability[39].

We then fit the following four different types of models to the data.

(1) A relativistic beaming model with $5 + 2 = 7$ model parameters: eccentricity e, argument of pericentre ω, amplitude K, phase t_0, and orbital period P, as well as the two noise parameters σ_D and τ_D.

(2) An accretion rate model with $3 + 2 = 5$ model parameters: amplitude K, phase t_0, and period P, as well as the two noise parameters σ_D and τ_D. This model assumes that the light curve of PG 1302-102 tracks the mass-accretion rates that are predicted in hydrodynamic simulations. For near-equal-mass binaries, several

studies have found that the mass-accretion rates fluctuate periodically, but resemble a series of sharp bursts, unlike the smoother, sinusoid-like shape of the light curve of PG 1302-102. To our knowledge, only three studies so far have simulated unequal-mass ($q \lesssim 0.1$) SMBH binaries[11,13,15]. The accretion rates for these binaries are less 'bursty'; among all of the cases in these three studies, the $q = 0.075$ and $q = 0.1$ binaries in ref. 11 resemble the light curve of PG 1302-102 most closely (see Extended Data Fig. 3). Here we adopt the published accretion curve for $q = 0.1$, and perform a fit to PG 1302-102 by allowing an arbitrary linear scaling in time and amplitude, as well as a shift in phase; this gives us the three free parameters for this model. (We find that the $q = 0.075$ case provides a worse fit.)
(3) A sinusoid model with $3 + 2 = 5$ parameters: amplitude K, phase t_0, and period P, as well as the two noise parameters σ_D and τ_D. This model is equivalent, to first order in v/c, to the beaming model restricted to a circular binary orbit.
(4) A constant luminosity model with 2 parameters, the noise parameters σ_D and τ_D. This model is for reference only, to quantify how poor the fit is with only these parameters.

In each of these models, we fixed the mean flux to correspond to the mean magnitude M that is inferred from the optical data; allowing the mean to be an additional free parameter did not change our results. The highest maximum likelihood is found for the beaming model, with best-fit values of $P = 1{,}996^{+29}_{-35}$ days, $K = 0.065^{+0.007}_{-0.006}c$, $e = 0.09^{+0.07}_{-0.06}$, $\cos(\omega) = -0.65^{+1.2}_{-0.06}$, and $t_0 = 718^{+422}_{-34}$ days, where the reference point t_0 is measured from MJD − 49,100. Uncertainties are computed with the 'emcee' code[40], which implements a Markov chain Monte Carlo algorithm, and which we use to sample the seven-dimensional posterior probability of the model given the data in ref. 6. We use 28 individual chains to sample the posterior for 1,024 steps each. Throwing away the first 600 steps ('burning in'), we run 424 steps and for each parameter we quote best-fit values corresponding to the maximum posterior probability, with errors given by the 85th and 15th percentile values (marginalized over the other six parameters). The best-fit noise parameters are $(\sigma_D, \tau_D) = (0.049^{+0.016}_{-0.001}$ mag, $37.6^{+35.2}_{-1.5}$ days). The best-fit model has a reduced $\chi^2/(N-1-7) \approx 2.1$, where $N = 245$ is the number of data points.

To assess which of the models is favoured by the data, we use the Bayesian information criterion (BIC), a standard method for comparing different models that penalizes models with a larger number of free parameters[41]. Specifically, $\mathrm{BIC} = -2\ln(\mathcal{L}) + k\ln(N)$, where the first term is evaluated using the best-fit parameters in each of the models and k is the number of model parameters. We find the following differences $\Delta\mathrm{BIC}$ between pairs of models:
$\mathrm{BIC}_{Acc} - \mathrm{BIC}_{Beam} = 4.0$ (the beaming model is preferred over the accretion model);
$\mathrm{BIC}_{Acc} - \mathrm{BIC}_{Sin} = 14.9$ (the sinusoid model is strongly preferred over the accretion model);
$\mathrm{BIC}_{Sin} - \mathrm{BIC}_{Beam} = -10.9$ (the sinusoid model is strongly preferred over the beaming model);
$\mathrm{BIC}_{Const} - \mathrm{BIC}_{Beam} = 11.5$ (the beaming model is strongly preferred over pure noise); and
$\mathrm{BIC}_{Const} - \mathrm{BIC}_{Sin} = 22.4$ (the sinusoid model is strongly preferred over pure noise).

We conclude that a sinusoid, or equivalently the beaming model restricted to a circular binary, is the preferred model. This model is very strongly favoured over the best-fit accretion model (see Extended Data Fig. 3), with $\Delta\mathrm{BIC} > 14.9$. For the assumed Gaussian distributions, this corresponds to an approximate likelihood ratio of $\exp(-14.9/2) \approx 5.7 \times 10^{-4}$. Although our best-fit beaming model has a small non-zero eccentricity, the seven-parameter eccentric model is disfavoured (by $\Delta\mathrm{BIC} = 11.5$) over the five-parameter circular case.

We conservatively allowed the amplitude of accretion-rate fluctuations to be a free parameter in the accretion models, but we note that the accretion-rate variability measured in hydrodynamic simulations exhibits large (order one) deviations from the mean, even for $0.05 < q < 0.1$ binaries[11,13,15]. In the accretion-rate model, an additional physical mechanism needs to be invoked to damp the fluctuations to the smaller, approximately 14% amplitude seen in PG 1302-102 (such as a more substantial contribution from the CBD and/or the primary).

Disk precession. The lowest BIC model, with a steady accretion rate and a relativistic boost from a circular orbit, has a reduced $\chi^2 = 2.1$, indicating that the relativistic-boost model with intrinsic noise does not fully describe the observed light curve. The residuals could be explained by a lower-amplitude periodic modulation in the mass-accretion rate, which is expected to have a non-sinusoidal shape (with sharper peaks and broader troughs, as mentioned above[13]). Alternatively, the minidisks, which we implicitly assumed to be co-planar with the binary orbit, could instead have a substantial tilt[12].

A circumsecondary minidisk that is tilted with respect to the orbital plane of the binary will precess around the binary angular-momentum vector, causing additional photometric variations due to the changing projected area of the disk on the sky. The precession timescale can be estimated from the total angular momentum

of the secondary disk and the torque exerted on it by the primary black hole. The ratio of the precession period to the orbital period of the binary is[42]

$$\frac{P_{prec}}{P_{orb}} = -\frac{8}{\sqrt{3}}\frac{\sqrt{1+q}}{\cos(\delta)}$$

where $\delta \in (-\pi/2, \pi/2)$ is the angle between the angular-momentum vectors of the disk and the binary, and we have chosen the outer edge of the minidisk to coincide with the Hill sphere of the secondary black hole $R_H = (q/3)^{1/3}a$, for binary semi-major axis a. This choice gives the largest secondary disk and the shortest precession rates. For small binary mass ratios, consistent with the relativistic beaming scenario, the precession can be as short as $4.8P_{orb}$, which causes variations on a timescale that spans the current observations of PG 1302-102. The precession timescale would be longer ($>20P_{orb}$) for a smaller secondary disk that is tidally truncated at $0.27q^{0.3}a$ (ref. 43), and with a more inclined ($45°$) disk.

Archival UV data. FUV (0.14–0.175 μm) and NUV (0.19–0.27 μm) spectra of PG 1302-102 were obtained by the HST and the GALEX since 1992. HST FOS NUV spectra were obtained on 17 July 1992 (pre-COSTAR)[44]. HST STIS FUV spectra were obtained on 21 August 2001 (ref. 45). GALEX FUV and NUV spectra were obtained on 8 March 2008 and 6 April 2009, and HST COS FUV spectra were obtained on 28 January 2011. All data are publicly available through the Mikulski Archive for Space Telescopes at http://archive.stsci.edu. All measurements were spectrophotometrically calibrated, and binned or smoothed to a resolution of 1–3 Å. The spectra (Fig. 2) have errors per bin that are typically less than 2%; published absolute photometric accuracies are better than 5%.

From each spectrum, average flux measurements (Fig. 2) were obtained in one or both of two discrete bands: FUV continuum (0.145–0.1525 μm; a range chosen to avoid the Lyα line) and NUV continuum (0.20–0.26 μm). For the GALEX NUV photometric data (also used in Fig. 2) we adopted a small correction (0.005 mag) for the transformation from the GALEX NUV to our NUV continuum band. GALEX FUV photometric data were not used because of the substantial contribution from redshifted Lyα. The broad lines in the UV spectra (in Fig. 3) do not show a large Doppler shift ($\Delta\lambda = (v/c)\lambda \approx 140$ Å). This is unsurprising, because the broad line widths (2,500–4,500 km s^{-1}) are much smaller than the inferred relativistic line-of-sight velocities, and are expected to be produced by gas at larger radii, unrelated to the rapidly orbiting minidisks that produce the featureless thermal continuum emission[22].

27. Richards, G. T. et al. Spectral energy distributions and multiwavelength selection of type 1 quasars. Astrophys. J. **166** (Suppl.), 470–497 (2006).
28. Yu, Q. & Tremaine, S. Observational constraints on growth of massive black holes. Mon. Not. Astron. R. Soc. **335,** 965–976 (2002).
29. Shakura, N. I. & Sunyaev, R. A. Black holes in binary systems. Observational appearance. Astron. Astrophys. **24,** 337–355 (1973).
30. Jiang, Y.-F., Stone, J. M. & Davis, S. W. A global three-dimensional radiation magneto-hydrodynamic simulation of super-Eddington accretion disks. Astrophys. J. **796,** 106 (2014).
31. Narayan, R. & McClintock, J. E. Advection-dominated accretion and the black hole event horizon. New Astron. Rev. **51,** 733–751 (2008).
32. Mahadevan, R. Scaling laws for advection-dominated flows: applications to low-luminosity galactic nuclei. Astrophys. J. **477,** 585–601 (1997).
33. Narayan, R., Mahadevan, R. & Quataert, E. in Theory of Black Hole Accretion Disks (eds Abramowicz, M. A. et al.) 148–182 (Cambridge Univ. Press, 1998).
34. Hutchings, J. B., Morris, S. C., Gower, A. C. & Lister, M. L. Correlated optical and radio structure in the QSO 1302-102. Publ. Astron. Soc. Pac. **106,** 642–645 (1994).
35. Wang, J.-M., Ho, L. C. & Staubert, R. The central engines of radio-loud quasars. Astron. Astrophys. **409,** 887–898 (2003).
36. Tanaka, T. & Menou, K. Time-dependent models for the afterglows of massive black hole mergers. Astrophys. J. **714,** 404–422 (2010).
37. Artymowicz, P. & Lubow, S. H. Dynamics of binary-disk interaction. 1. Resonances and disk gap sizes. Astrophys. J. **421,** 651–667 (1994).
38. Kozłowski, S. et al. Quantifying quasar variability as part of a general approach to classifying continuously varying sources. Astrophys. J. **708,** 927–945 (2010).
39. Andrae, R., Kim, D.-W. & Bailer-Jones, C. A. L. Assessment of stochastic and deterministic models of 6304 quasar lightcurves from SDSS Stripe 82. Astron. Astrophys. **554,** A137 (2013).
40. Foreman-Mackey, D., Hogg, D. W., Lang, D. & Goodman, J. emcee: the MCMC hammer. Publ. Astron. Soc. Pac. **125,** 306–312 (2013).
41. Kass, R. E. & Raftery, A. E. Bayes factors. J. Am. Stat. Assoc. **90,** 773–795 (1995).
42. Lai, D. Star-disc-binary interactions in protoplanetary disc systems and primordial spin-orbit misalignments. Mon. Not. R. Astron. Soc. **440,** 3532–3544 (2014).
43. Roedig, C., Krolik, J. H. & Miller, M. C. Observational signatures of binary supermassive black holes. Astrophys. J. **785,** 115 (2014).
44. Evans, I. N. & Koratkar, A. P. A complete atlas of recalibrated Hubble Space Telescope Faint Object Spectrograph spectra of active galactic nuclei and auasars. I. Pre-COSTAR spectra. Astrophys. J. **150** (Suppl.), 73–164 (2004).
45. Cooksey, K. L., Prochaska, J. X., Chen, H.-W., Mulchaey, J. S. & Weiner, B. J. Characterizing the low-redshift intergalactic medium toward PKS 1302–102. Astrophys. J. **676,** 262–285 (2008).
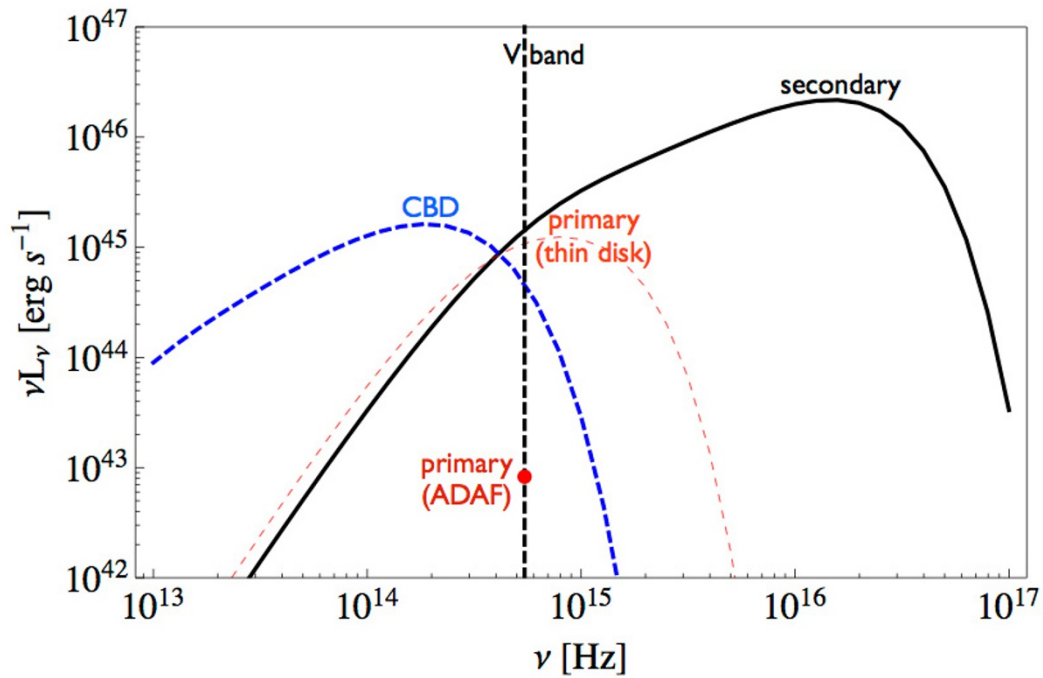
Extended Data Figure 1 | Model spectrum of PG 1302-102. Circumbinary (dashed blue) and circumsecondary (solid black) disk spectra for a total binary mass of $10^{9.4}M_\odot$, binary mass ratio of $q = 0.05$, and ratio of accretion rates $\dot{M}_2/\dot{M}_1 = 20$. A vertical dashed line marks the centre of the V band and the approximate flux from an advection-dominated accretion flow (ADAF) is shown as a red dot for the V-band contribution of the primary. The spectrum for a radiatively efficient, thin disk around the primary is shown by the thin red dashed curve for reference.
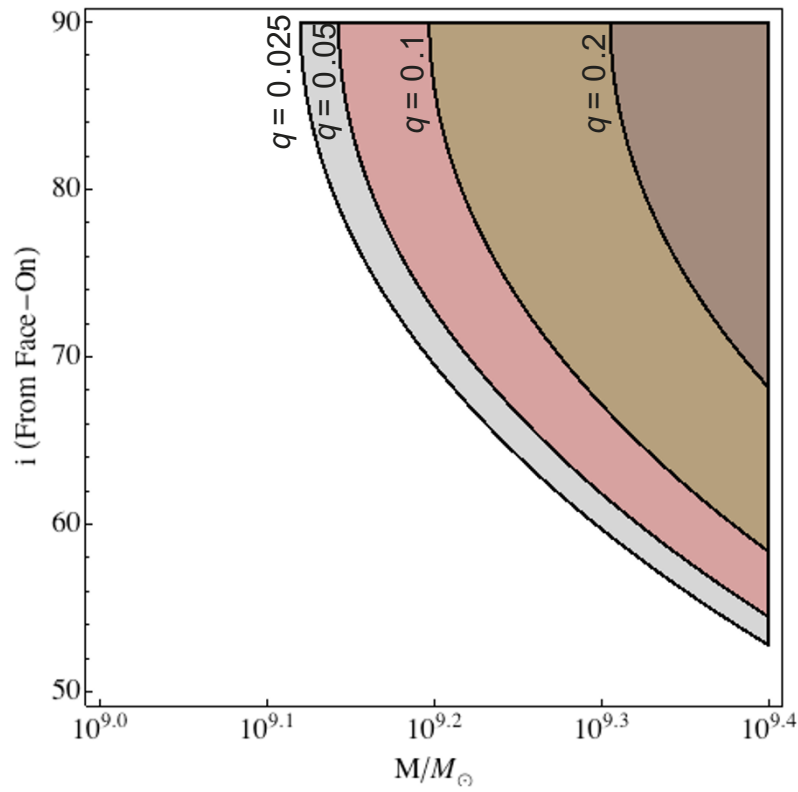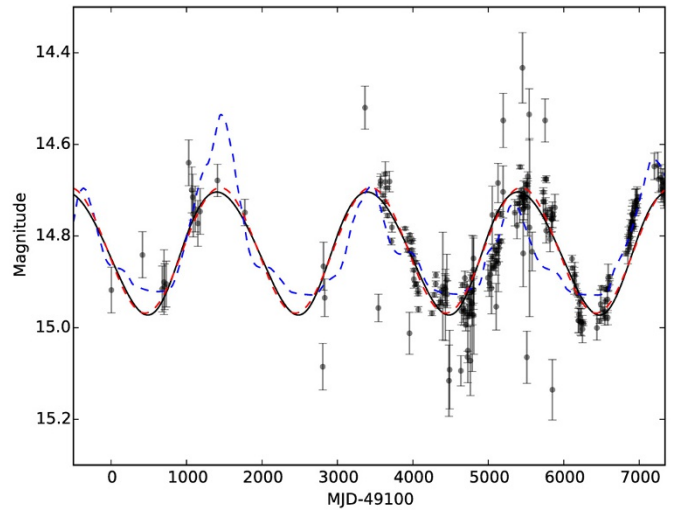
Extended Data Figure 2 | Parameter combinations for which the combined V-band luminosity of the three-component system varies by the required 0.14 mag. M is the binary mass, q is the mass ratio, and i is the orbital inclination angle. This figure is analogous to Fig. 1, except instead of adopting an ad-hoc fractional luminosity contribution f_2 by the secondary, the luminosities of each of the three components are computed from a model: the luminosity of the primary is assumed to arise from an ADAF, whereas the luminosity of the secondary is generated by a modestly super-Eddington thin disk. Emission from the circumbinary disk is also from a thin disk, and is negligible except for binaries with the lowest mass ratio $q \lesssim 0.01$ (see text).
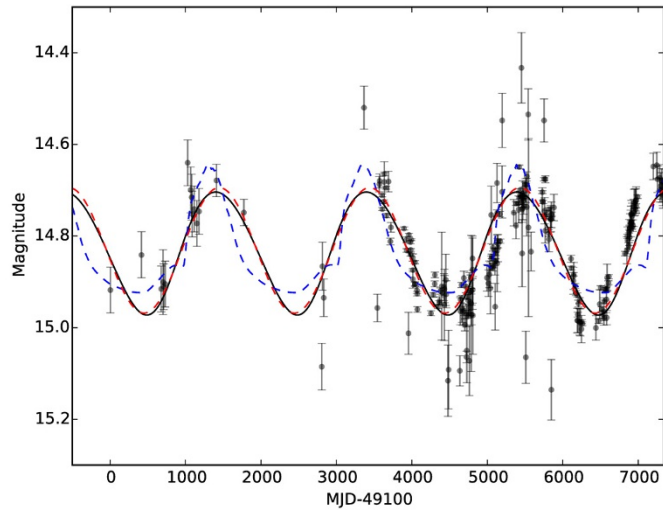
Extended Data Figure 3 | Model fits to the optical light curve of PG 1302-102. Best-fit curves assuming relativistic boost from a circular binary (solid black curves), a pure sinusoid (red dotted curves), and accretion rate variability adopted from hydrodynamic simulations[11] (blue dashed curves) for a $q = 0.075$ (left) and a $q = 0.1$ (right) binary. The grey points with 1σ error bars are the data for PG 1302-102 (ref. 6).